

High resolution in situ mapping of microstrain and microstructure evolution reveals damage resistance criteria in dual phase steels



Dingshun Yan, Cemal Cem Tasan*, Dierk Raabe

Max-Planck-Institut für Eisenforschung GmbH, Max-Planck-Str. 1, 40237 Düsseldorf, Germany

ARTICLE INFO

Article history:

Received 7 February 2015

Revised 25 May 2015

Accepted 25 May 2015

Available online 29 June 2015

Keywords:

Dual-phase

Damage

In situ

Digital image correlation

EBSD

ABSTRACT

Microstructures of multi-phase alloys undergo morphological and crystallographic changes upon deformation, corresponding to the associated microstructural strain fields. The multiple length and time scales involved therein create immense complexity, especially when microstructural damage mechanisms are also activated. An understanding of the relationship between microstructure and damage initiation can often not be achieved by post-mortem microstructural characterization alone. Here, we present a novel multi-probe analysis approach. It couples various scanning electron microscopy methods to microscopic-digital image correlation (μ -DIC), to overcome various challenges associated with concurrent mapping of the deforming microstructure along with the associated microstrain fields. For this purpose a contrast- and resolution-optimized μ -DIC patterning method and a selective pattern/microstructure imaging strategy were developed. They jointly enable imaging of (i) microstructure-independent pattern maps and (ii) pattern-independent microstructure maps. We apply this approach here to the study of damage nucleation in ferrite/martensite dual-phase (DP) steel. The analyses provide four specific design guidelines for developing damage-resistant DP steels.

© 2015 Acta Materialia Inc. Published by Elsevier Ltd. All rights reserved.

1. Introduction

The drive toward improved combinations of high strength and ductility motivates the design of novel alloys with complex, multi-phase micro-/nano-structures. Many of the recently introduced alloys demonstrate this microstructural complexity, containing multiple phases of different composition, crystallography, morphology, dispersion, stability and size. Examples are ultrafine-grained α/α' dual-phase (DP) steel [1], α'/γ transformation-induced plasticity (TRIP) steel [2], Triplex steel [3], TRIP-maraging steel [4], β/α titanium alloys [5] and α/X magnesium alloys [6]. Some of them are shown in Fig. 1. Such alloys present a composite-like micro-mechanical response, which in turn enables tuning optimal combinations of strength and ductility by adjusting the phase fractions as well their individual properties, interfaces and morphology.

However, incorporating phases of high mechanical contrast promotes the risk of micro-cracking at spots of high stress and/or strain mismatch. This in turn may cause early mechanical softening, or even catastrophic failure. Due to these reasons, damage evolution has been intensively studied in recent years

especially in DP steels [7–13]. Most common damage sites in DP steels are the martensite/ferrite interfaces (**M/F**) or martensite island interiors (**M**) [9]. However, there are different views on exactly how these mechanisms nucleate and interact with each other. Kang et al. [10] and Avramovic et al. [7] both reported that the early-stage damage incidents are initiated inside **M** prior to percolative plastic instability, while other damage mechanisms are activated following such mesoscale localization phenomena. However, Avramovic et al. [7] also noted that **M/F** damage incidents play a more critical role for the overall properties. Maire et al. observed a more balanced damage activity of **M/F** and **M** [11]. Recently, Hoefnagels et al. have carried out an extensive analysis through quantitative characterization of the influence of the starting microstructure, strain path and strain level on the resulting damage mechanisms [9]. The obtained experimental and simulation results were explained in terms of a hypothesis that proposes that the two mechanisms are intrinsically coupled, i.e., the **M/F** damage incidents are typically initiated by **M** cracking.

These contradicting views arise from the insufficient resolution in the analysis of deformation and damage at the same position, with respect to their strong heterogeneity at microstructure-scale [8,12,13]. Thus, it is required to introduce novel analysis methods, which make use of advanced high resolution probing techniques of micro-mechanical processes during deformation. However, this is

* Corresponding author. Tel.: +49 211 6792 866; fax: +49 211 6792 333.

E-mail address: c.tasan@mpie.de (C.C. Tasan).

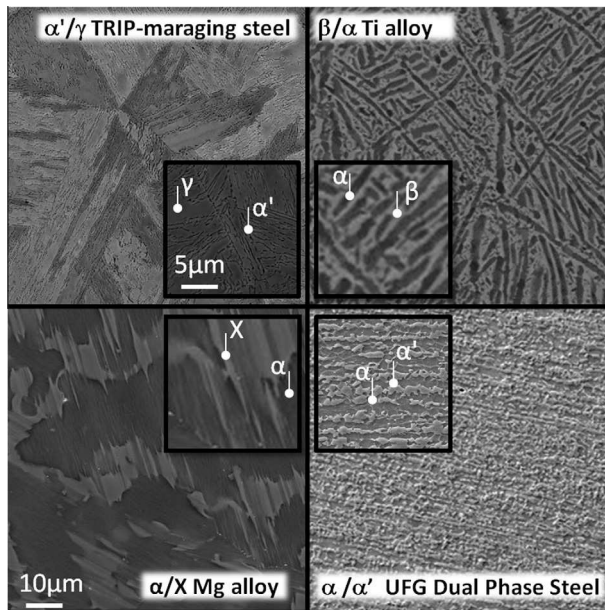


Fig. 1. Dual-phase microstructures of some recently introduced bulk nanostructured alloys: TRIP-maraging steel (courtesy of Meimei Wang), β/α titanium alloys (courtesy of Zahra Tarzimaghadam), α/X magnesium alloys (courtesy of Jinkyung Kim) and ultrafine-grained α/α' dual-phase steel. Phases are marked in the zoomed-in insets.

an experimental task that imposes multiple challenges, as it requires the simultaneous mapping of the deformation-induced evolution of the (i) microstructure, (ii) microstrain and (iii) micro-stress fields at a representatively large field-of-view and yet, a sufficiently high spatial resolution.

Here, we present new insights into damage nucleation in DP steels by developing a novel methodology that overcomes challenges (i) and (ii).¹ This methodology combines in-situ scanning electron microscopy (SEM) testing with optimized microscopic-digital image correlation (μ -DIC) analysis. In this regard, the following report is divided into three parts. Part-A, “Methodology Development”, presents a detailed overview of the currently existing approaches, to motivate the need for introducing an advanced methodology, and to point out the ingredients of the optimal strategy in that context. In Part-B “Proof-of-Principle”, a detailed description and assessment of the introduced coupled microstrain and microstructure mapping ($\mu\epsilon$ & μS mapping) methodology is presented. Finally in Part-C, “Case Study”, the developed method is applied to investigate damage evolution in DP steel with the final aim to identify guidelines for designing damage-resistant microstructures.

PART-A

2. Methodology development

2.1. Challenges in coupled $\mu\epsilon$ & μS mapping in SEM

For challenge (i), i.e. mapping deformation-induced microstructure evolution, SEM is the ideal observation tool due to two main reasons. First, it allows the operation of multiple imaging detectors

¹ The microstructure and microstrain fields obtained in the presented approach also enable a numerically-assisted indirect solution for challenge (iii), i.e. the associated stress field calculations. This aspect is discussed in detail elsewhere though [14].

Table 1

Imaging modes in SEM environment that allow investigation of different micro-mechanical phenomena.

Imaging Mode	Micro-mechanical phenomena
Secondary Electron	Damage mechanisms [10,19], slip trace analysis [20], surface roughening [21], shear banding [22], etc.
BackScattered Electron, Electron Channeling Contrast Imaging	Dislocation imaging [23,24], sub-grain formation [25,26], mechanical twinning [27,28], phase transformation [29], etc.
Electron BackScatter Diffraction	Micro-texture [30,31], phase transformation [32–34], defect density [35], sub-grain formation [36,37], slip trace analysis [38], etc.

that are capable of probing a set of relevant micro-mechanical phenomena (Table 1) at an optimal combination of spatial resolution and field-of-view. In this regard, recent developments in electron backscatter diffraction (EBSD) and electron channeling contrast imaging (ECCI) techniques are of specific significance, as they enable current SEM's to deliver quantitative, spatially-resolved mapping of crystallographic features and defects [15,16], even single dislocations [17]. Second, with respect to techniques that provide improvements in spatial resolution, e.g., transmission electron microscopy, or in 3D analysis capabilities, e.g., X-ray micro/nano-tomography [11,18], requirements on sample size, surface quality, and imaging are far less stringent. This flexibility strongly helps imposing well-defined deformation boundary conditions and implementation of a multi-probe imaging approach.

For tackling challenge (ii), i.e. mapping deformation-induced microstrain evolution, the recently introduced μ -DIC approach is the ideal route since it provides the most direct coupling to high resolution microstructure maps obtained during deformation [19,39]. DIC requires registering and correlation of a random pattern to calculate displacement fields and from these the corresponding strain maps [40,41]. While DIC is typically used with optical camera images [42–44], μ -DIC is based on images from a microscope. Principally image series from any microscope can be used for μ -DIC. However, considering the spatial resolution and field-of-view requirements, and the need for direct coupling to deformation-induced microstructure evolution, SEM based μ -DIC [19,45] excels as the ideal approach with respect to other alternatives, e.g., optical microscopy [46] and atomic force microscopy [47].

While SEM is identified as the ideal medium for microstructure or microstrain mapping, challenges arise when coupling them. These shortcomings are next summarized by categorizing the previous such efforts into two groups based on the nature of the DIC pattern on the sample, namely, using microstructure-based patterns on the one hand vs. artificial patterns on the other hand. For these groups, Fig. 2 schematically demonstrates the evolution of the pattern and the corresponding μ -DIC and EBSD maps at different deformation levels.

The first group relies on tracking specific microstructural features for correlation. Examples are slip traces in BSE [48] or SE [45] images, and especially boundaries in SE images of etched microstructures [10,19,49,50] or in EBSD image quality maps [51]. Owing to its practicality, this approach is the most popular microstrain mapping strategy, despite several, often overlooked, limitations: First, as pointed by arrow-1 in Fig. 2, etching causes considerable undesired microstructure manipulation, such as grain boundary grooving, that may alter the true strain field through local stress intensification. Second, as indicated by arrow-2 in Fig. 2, spatial strain resolution of these approaches is intrinsically coupled to the average grain size, and hence, is often insufficient to resolve in-grain strain heterogeneities. Moreover, as shown by

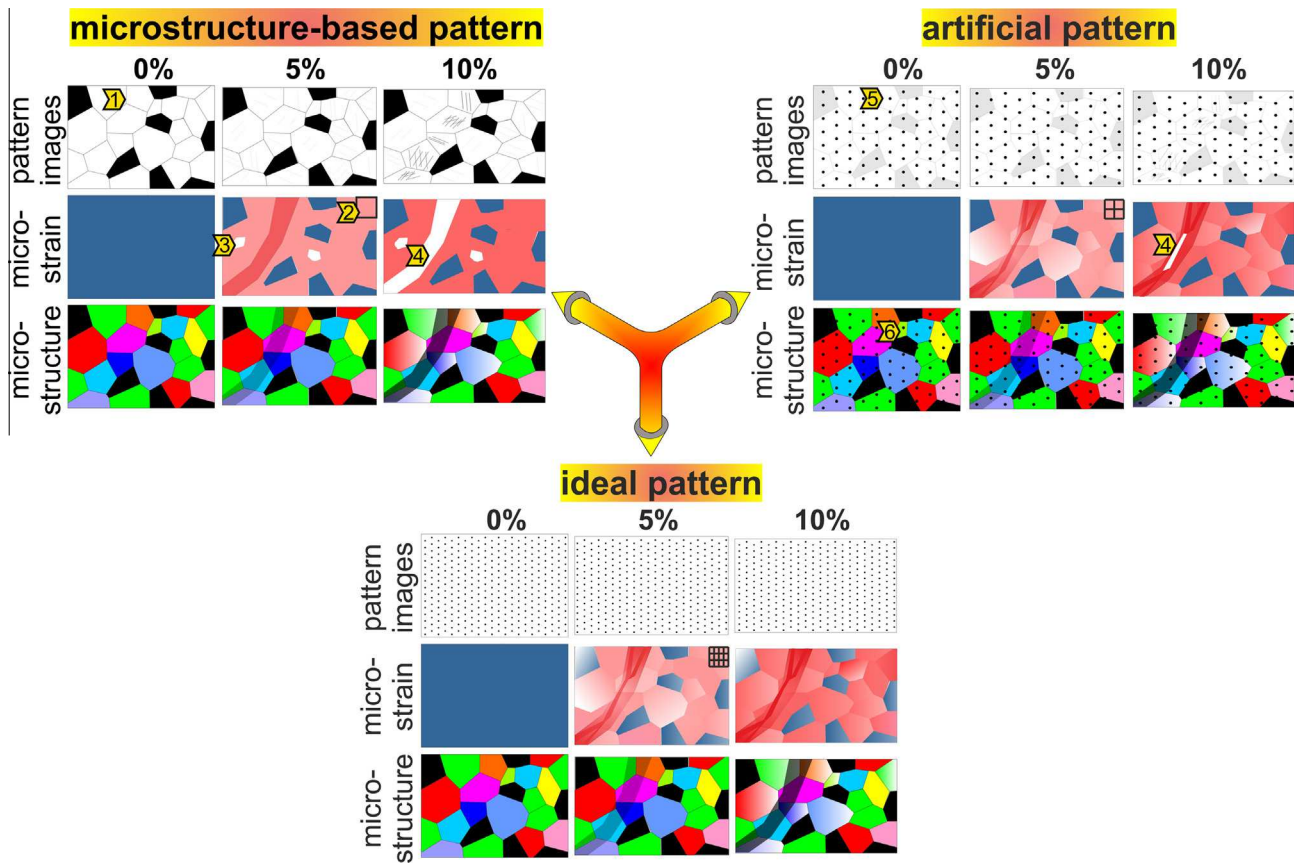


Fig. 2. Schematic comparison of the microstructure-based, artificial and ideal μ -DIC pattern strategies, for the example of the deformation of ferrite/martensite DP steel. Here, the pattern images are the input and the microstrain images are the output of the DIC analysis; and the microstructure images represent the output of EBSD analysis. DIC facet sizes are indicated at the upper right corner of 5% microstrain maps. White regions in the micro-strain maps correspond to those regions where DIC fails. Microstructure-based patterns suffer from preparation-induced microstructure manipulation (arrow 1) and low spatial resolution (arrow 2), and produce incomplete strain maps (arrows 3 and 4). Artificial patterns suffer from preparation-induced microstructure manipulation (arrow 5), and produce incomplete strain maps (arrow 4) and incomplete microstructure maps (arrow 6).

arrow-3 in Fig. 2, even at low deformation levels, strain maps are typically already incomplete due to the feature-free grain interiors. As pointed by arrow-4 in Fig. 2, this problem is intensified at higher deformation levels due to the strong detrimental effect of deformation-induced grain rotations, phase transformations, surface roughening, etc.

The second group, i.e. artificial patterning methods, relies on the application of a contrast agent on the surface. This is done by processes such as direct [52,53] or indirect [54] focused ion beam (FIB) milling; electron beam [39,55–58] or ultraviolet [59] lithography; physical vapor deposition followed by rearrangement via chemical vapor exposure [59,60] or solid state dewetting [61], or with masks for Au pattern [62]; electron beam-induced deposition (EBID) of Pt [63]; or nanoparticle (NP) deposition of Au [64,65] or Pt [66]. These approaches provide significant improvements in terms of the spatial resolution and completeness of μ -DIC strain maps. However, as indicated by arrow-5 in Fig. 2, microstructure manipulation is inevitably introduced due to direct FIB milling effects [67,68] or the associated heat treatments. Examples are chemical vapor exposure at 60–160 °C for 1–24 h [59], or solid state dewetting at 300 °C for 5 min [61]. Moreover, as pointed by arrow-6 in Fig. 2, microstructure information is lost where the pattern agent stands, since the large-atomic-number noble-metal deposits² heavily

backscatter the beam electron and in turn limit its penetration depth. Correlation issues, as indicated by arrow-4 in Fig. 2, and their low practicality (e.g. arising from FIB milling, lithography and EBID methods being limited to small areas) further limit the overall applicability of these approaches.

In summary, both types of patterning approaches manipulate the underlying microstructure and cannot exclude the undesired microstructure influence on the pattern. Artificial pattern-based approaches provide relatively higher resolution microstrain maps, but at the expense of more severely interfering with the microstructure maps.

2.2. Proposed strategy for coupled $\mu\epsilon$ & μS mapping in SEM

We propose that the limitations explained above can be overcome if the patterns and the microstructure can be “selectively imaged” during deformation, i.e. independent of each other (see the “ideal case” in Fig. 2). The main methodological requirements associated with such an improved approach are:

- to achieve high spatial strain resolution, particles that are at least two orders of magnitude below the micrometer scale need to be identified and dispersed in a highly-dispersed pattern on the sample surface before deformation (criterion-A);
- to enable selective microstructure imaging, (i) pattern influences on microstructure mapping should be avoided by choosing amorphous, nano-sized particles that can be dispersedly deposited as a single layer, and (ii) microstructure manipulation

² Among artificial patterning methods, particle deposition strategies replacing noble metal with 1 μm sized Si [46], 5 μm sized Ti [69], and 20 nm [70–72] or 150 nm [73] sized SiO_2 avoid this problem, although these applications were carried under optical microscope.

by the particles should be avoided by choosing chemically-inert nano-particles which can be deposited without additional temperature exposure (criterion-B);

- to enable selective pattern imaging, the SEM imaging conditions need to be optimized for low-interaction volume imaging with minimized edge and charging effects. This ensures particle imaging independent of diffraction and topographic contrast effects (criterion-C).

Matching these three conditions required conducting an extensive optimization study in terms of the employed nanoparticles, dispersion methodology and SEM imaging conditions. We found that employing (1) SiO₂ nanoparticles; (2) a modified drop casting methodology and; (3) in-lens SE imaging with optimized SEM beam parameters fulfills all three conditions. Details and optimization procedures are provided in [Appendix A](#).

Part-B

3. Proof-of-principle: experimental details

Experimental details of both, proof-of-principles tests, and the application of the $\mu\epsilon$ & μS mapping method outlined above to damage analysis in DP800 tensile test specimens (with gauge dimensions $5 \times 1 \times 0.5$ mm) will be presented in the following sections. SEM analyses are carried out using a Zeiss 1540XB Crossbeam FIB-SEM. This instrument is equipped with an EDAX/TSL system used for EBSD measurements at a step size of 100 nm. The tensile test specimens are deformed stepwise using a Kammrath & Weiss tensile stage at $3 \mu\text{m/s}$ constant cross head speed corresponding to an initial strain rate of $6 \times 10^{-4} \text{ s}^{-1}$. At different deformation steps, four representative areas each sized $18 \times 13 \mu\text{m}$ are mapped using SE, BSE and EBSD detectors, and the nanoparticle patterns are mapped using an in-lens SE detector. To avoid problems arising from hydrocarbon contamination,³ plasma cleaning is conducted after EBSD scanning. Each detector provides input with respect to different aspects of the damage nucleation phenomena: While SE images are used to consider surface roughness, in-lens SE images are used both for the identification and tracking of early-state nano-cracks and for carrying out DIC to determine local strain fields and strain gradients associated with damage incidents. EBSD provides maps of the local microstructure and of the crystallographic orientation gradients surrounding damage incidents. Further, it enables a qualitative assessment of heterogeneities in local stress distribution based on the positive correlation of the local stress to the total dislocation density (i.e. the sum of statistically stored dislocation (SSD) and GND densities [74]). When plausibly assuming that the initial SSD density is very small, it can be reduced to its deformation-induced contribution, rendering it related to the local strain. The GND density can be derived from the local orientation gradients [75], or from strain gradients and initial orientation gradients.⁴

³ Hydrocarbon contamination not only reduces the contrast among particles and the background, but also introduces additional surface charging. As the optimized pattern imaging method is very sensitive to surface condition, this contamination deteriorates the pattern imaging and introduces absolute errors in strain mapping by $\pm 0.2\%$ per 15min imaging. It is also observed that hydrocarbon contamination enhances the adherence of particles on the specimen, as also documented in [64]. Therefore, plasma cleaning is important if the particles are to be removed.

⁴ There are known sources of error in these analyses. As the collected DIC and EBSD data are not depth-resolved, the calculated gradients are only valid in 2D, which leads to an error in the calculated GND density [75]. Also, since the strain resolution (100 nm) is typically larger than the early stage crack size (~ 10 nm), local strains at damage incidents can be underestimated. The studied local strain at damage nucleation (the critical strain) is the average of local strain just before and after damage nucleation. Presented error bar is for these two bounds.

After deformation, to compensate for the absence of topological information, the subsurface microstructure effects on the surface $\mu\epsilon$ & μS maps are investigated by depth-controlled post-mortem serial sectioning and follow-up EBSD measurements. The procedure is carried out with colloidal silica (OPS) polishing rather than with FIB, to obtain a larger field of view.

The Aramis software (V6.3.0, GOM GmbH) is employed to perform DIC based on in-lens SE images. An optimization study was carried out to identify ideal values for the main accessible parameters, namely, (1) facet size, (2) facet overlap, (3) number of start points and (4) choice of reference state. For the following analysis the facet size has been set to the same value (100 nm) as the EBSD square grid step size for the direct coupling to microstructure measurements and corresponding full-field crystal plasticity simulations [14,76]. The remaining DIC parameters are not further optimized despite possible improvements in correlation performance. Considering further that the in-lens SE images are directly used without image post-processing, the presented data can be regarded as lower-bound results in terms of the success of the DIC analysis. An equivalent strain definition (von Mises) is used here for the plots due to its positive correlation to SSD density.

4. Proof-of-principle: results

Next we present the proof-of-principle results to demonstrate that the three critical conditions (see section above) are all successfully met by the developed methodology. More details on how this methodology, which is based on drop casting of SiO₂ nanoparticles and in-lens SE imaging with optimized electron beam parameters, fulfills these three conditions is explained in more detail in [Appendix A](#).

4.1. Selective microstructure and pattern imaging

The modified drop casting protocol successfully avoids delivering stacked, agglomerated or too-widely spaced SiO₂ deposits ([Fig. 3a₁–a₃](#)) that would interfere with the coupled $\mu\epsilon$ & μS mapping methodology (see [Appendix A](#)). Instead, it provides a well-dispersed monolayer, as shown in [Fig. 3a₄](#) and also the magnified inset therein. Besides, for exactly the same area as in [Fig. 3a₄](#), microstructure images, such as the BSE and the ECCI images in [Fig. 3b](#) and the EBSD maps in [Fig. 3c](#), show no obvious pattern effects. Thus, selective microstructure imaging is successfully achieved.

Next we focus on achieving selective pattern imaging. [Fig. 3a₄](#) reveals that a conventional SE detector cannot provide selective pattern imaging since microstructure effects create additional contrast. As shown in [Fig. A1](#) in [Appendix A](#), contributions from surface tilt variations and crystallographic orientation differences lead to a non-homogeneous background, and sometimes even fully hinder the imaging of particles. [Fig. 4a](#) clearly shows examples for both effects by conventional SE imaging of a highly deformed area.

The optimization of the selective pattern imaging conditions are achieved through three steps: [Fig. 4b](#) shows that decreasing voltage, current density and aperture aid in lowering the background contrast, especially the diffraction contrast. [Fig. 4c](#) shows that when using the SE detector in an in-lens position, the resulting image yields only limited background contrast, and especially the topological contrast is reduced. Finally, [Fig. 4d](#) shows that combining the above modifications yields a high contrast pattern image with homogeneous background. The progress enabled through these conditions is striking, as is revealed by the fact that [Fig. 4a–d](#) are all taken from exactly the same deformed region. This is important especially for multi-phase materials such as DP steels since these alloys are prone to develop pronounced surface

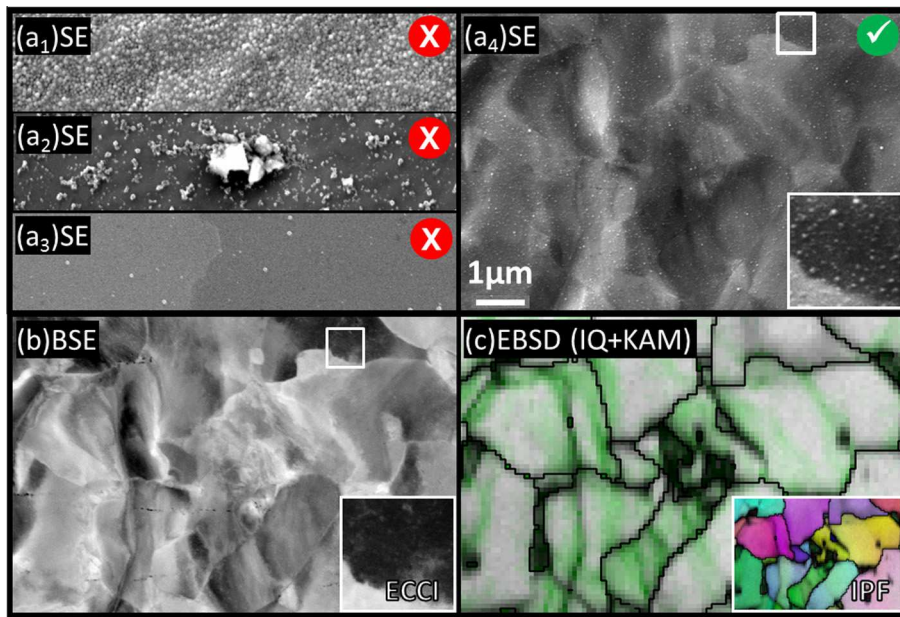


Fig. 3. Examples of unsuccessful (a_1 – a_3) and successful (drop cast) (a_4) SiO_2 particle deposition results. SE (inset cropped SE) (a_4), BSE (inset ECCI) (b), and EBSD – IQ + KAM (inset EBSD-IPF) (c) images of the same, deformed area demonstrate that the pattern is visible only in SE imaging mode.

topographies due to the inherent high mechanical contrast between the soft (e.g. ferrite) and the hard (e.g. martensite) phases.

4.2. Coupled $\mu\epsilon$ & μS mapping

To demonstrate the $\mu\epsilon$ & μS mapping technique, a specific probed area on a tensile-deformed specimen is tracked in Fig. 5. Columns 1–5 in Fig. 5 show SE, BSE, EBSD – IPF + IQ, in-lens SE and DIC maps, respectively. Row a–c in Fig. 5 show the evolution of these maps at 0, 0.08 and 0.15⁵ tensile strain, respectively.

Despite the deposited pattern, SE, BSE and EBSD analyses indeed reveal pattern-independent microstructure maps that enable us to study multiple micromechanical processes. For example, the topographic contrast obtained in SE or in-lens SE imaging mode can help to reveal damage incidents; the channeling contrast visible in the BSE images enables probing the ferrite substructure; and the EBSD data reveal the martensite sub-structure, to name but a few of the jointly accessible features. Yet, irrespective of these deformation-induced surface roughening effects (see, e.g., Fig. 5b₁), in-lens SE imaging provides microstructure-independent and featureless pattern maps which enable us to derive the local deformation fields at high fidelity up to severe strain levels (Fig. 5b₄). Thus, the resulting lower-bound DIC map has only few missing facets (Fig. 5b₅).

To provide a better impression of the achieved resolution, Fig. 5 also shows crops of the white framed area, denoted by the subscript ‘a’. Fig. 5b_{1a} shows strong surface topography after the nucleation of the damage incident, which normally renders the evaluation of actual damage incidents and local strain exceedingly difficult. Despite this severe local deformation, Fig. 5b_{4a} shows the in-lens SE image with no additional contrast except for those regions that are due to the actual damage incident. Details of how in-lens SE imaging enables this analysis are presented in Appendix A. Fig. 5b_{5a} shows that the corresponding strain map successfully captures the strain localization at the onset of this damage incident. With further deformation, Fig. 5c_{4a} shows that the

local strain at the boundaries of the damage incident can still be captured, but not within the newly opened crack surface.

The power of the coupled methodology lies in the possibility to refer back to the (pattern-independent) microstructure images to identify causes of micro-scale strain localization events. For example, for the white framed damage incident, Fig. 5b_{3a} and Fig. 5d shows the surface and sub-surface microstructure, respectively. This reveals that the damage incident initiates from the narrow section of a thin martensitic region positioned on a layer of sub-surface ferrite grains.

Altogether these results show that high fidelity and high resolution strain maps can be reliably obtained up to high strain levels in a high-mechanical contrast material, even in cases where damage incidents nucleate. This essential progress in the joint micromechanical and microstructural mapping technique, capable of identifying local micromechanics plus local damage incidents, is enabled by selective in-lens SE pattern imaging as well as by a clearer visualization of damage incidents compared to conventional SE images (see Fig. 7 for the apparent damage sensitivity of the in-lens SE images). Fig. 6 shows the resolution and the field-of-view as achieved by the methodology presented here in comparison to other strain mapping methods described in the literature,⁶ using the product of facet size in space (F_S) and in pixel (F_P) as parameters. The value achieved by the methodology introduced here, i.e., 100 nm in 17 pixels (even employing lower bound μ -DIC conditions), is among the lowest three values reached up to now. The potential of the method is further increased due to its applicability at high strains and to materials with high mechanical contrast.

PART-C

5. Case study: damage nucleation in ferrite/martensite DP steel

Here the high resolution $\mu\epsilon$ & μS mapping methodology is used for identifying critical microstructural parameters for damage nucleation in DP800 steel.

⁵ Due to necking, the local strain at this stage ($\epsilon_{\text{local}} = 0.23$) is higher than the tensile strain ($\epsilon_t = 0.15$).

⁶ Detailed μ -DIC conditions in other works cannot be accessed in all cases.

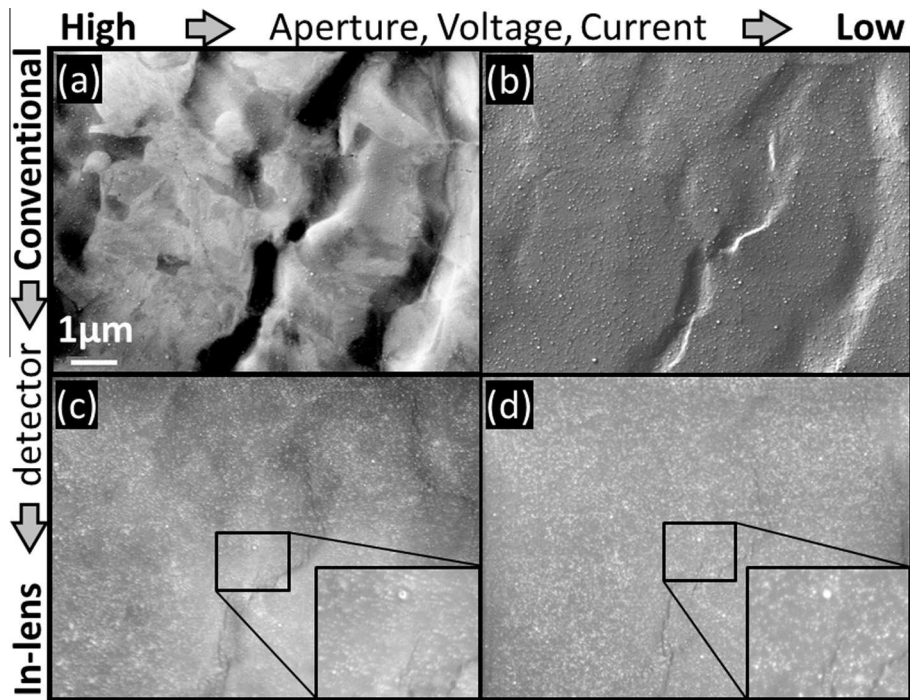


Fig. 4. Optimization of the imaging conditions for microstructure-independent pattern imaging: (a) conventional SE image of a deformed area with effects arising from undesired topographic and diffraction contrast; (b) optimization of imaging parameters decreases diffraction contrast (see details in [Appendix A](#)); (c) use of in-lens SE detector decreases topographic contrast; (d) fully optimized image mapping practically exclusively the pattern contrast (compare e.g. cropped (c) and (d) insets).

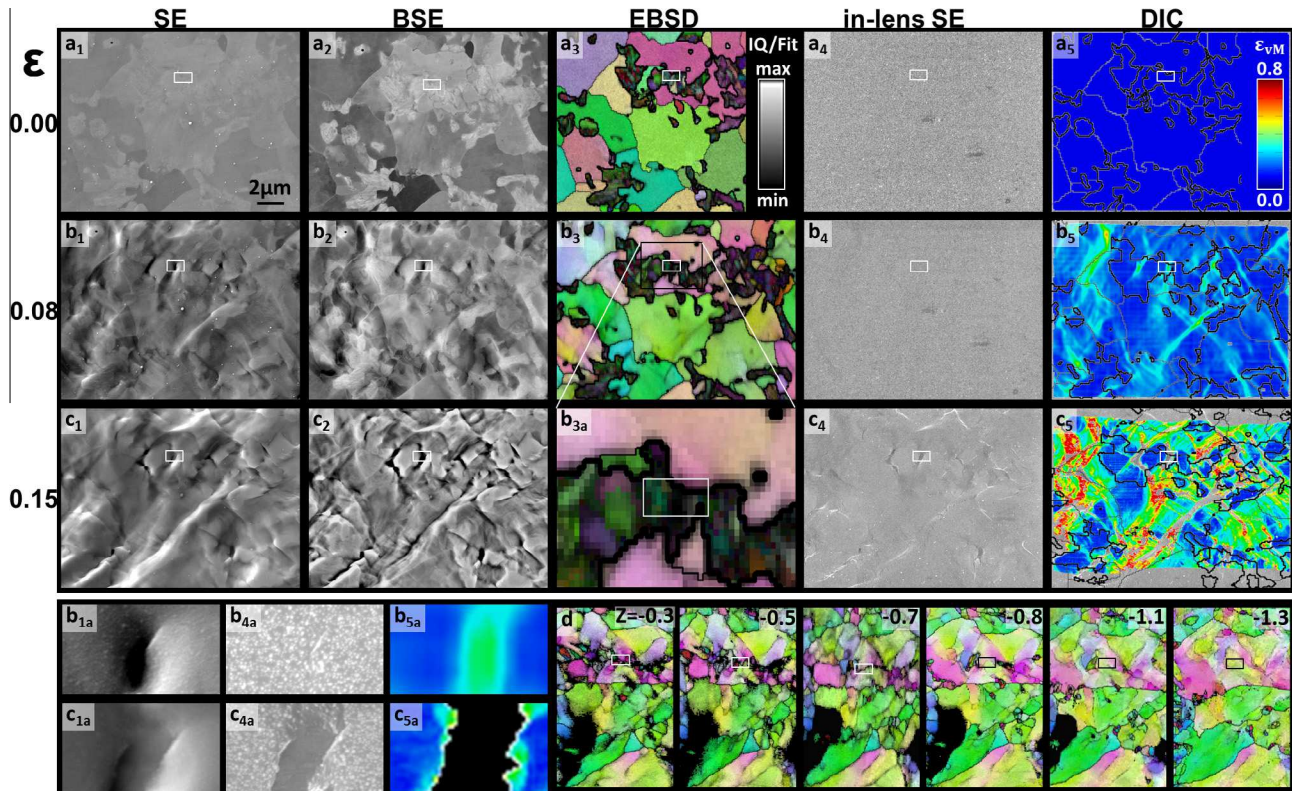


Fig. 5. Results of the coupled $\mu\epsilon$ & μS mapping methodology applied to DP steel at (a) 0, (b) 0.08 and (c) 0.15 tensile strain. Corresponding SE, BSE, EBSD – IPF + IQ + Boundary, in-lens SE and DIC images are shown respectively in column 1–5. SE, in-lens SE and DIC images corresponding to a damage incident (from the area marked by the white box in all sub-figures) are shown in (b,c)_{(1,4,5)a}. Results of the post-mortem serial sectioning showing the microstructure underneath in terms of EBSD – IPF + Fit maps are given in (d), where the through-thickness position Z is given in μm .

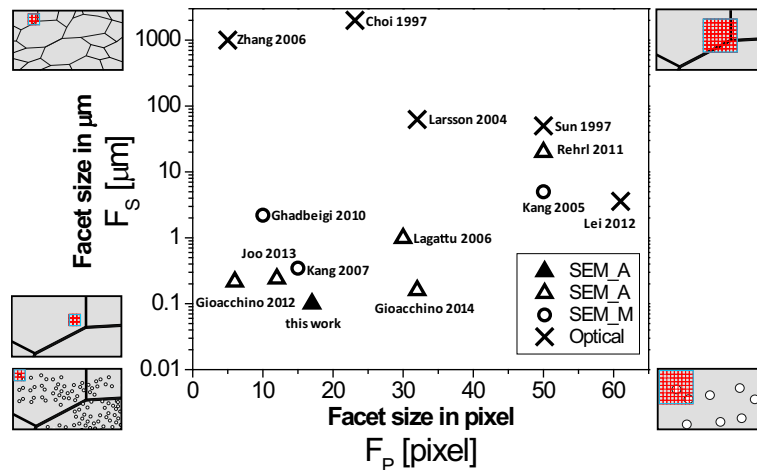


Fig. 6. μ -DIC facet size in pixel (F_p) versus facet size in μm (F_s) achieved in the literature by optical (cross) [69,77–80] and SEM imaging (open circle: microstructure-based pattern (M) [10,45,49], open triangle: artificial pattern (A) [60,61,63,81,82]), and in this paper by SEM imaging (closed triangle). Small product of $\ln(F_s)$ and F_p is ideal. Insets illustrate the challenges in using both small F_s and F_p (left bottom corner insets) at a certain image size and certain microstructure (with and without particle layer), comparing left bottom corners insets to insets at other corners. The red grids represent pixels, blue grids represent μ -DIC facet, open circle represent pattern particles, and black lines represent grain boundaries. For example, for the same F_s , pattern features are smeared out at small F_p ; and for the same F_p , few pattern features are included in one facet at small F_s .

5.1. Active damage mechanisms

As seen in the local strain maps in Fig. 5b₅,c₅ and the zoom-in shown in Fig. 9b₁,c₁, the plastic deformation is predominantly localized inside the ferrite, especially in narrow ferrite channels extended between larger martensitic regions. In conjunction with this observation, the spatial distribution of ferrite and martensite is observed to be the main factor influencing the damage process, rather than their crystallographic orientation. Thus, the identified active damage mechanisms are based on different local ferrite/martensite configurations: Damage inside ferrite grains is indicated by **F**; Damage inside the martensite islands is referred to as **M**; Damage at the ferrite grain boundary is referred to **F/F**; Damage at the martensite/ferrite phase boundaries is referred to **M/F**. The **M/F** category is further divided into damage events at ferrite channels and those occurring at martensite notch sites, which are referred to **M/F/M** and $\text{M}^{\text{E}/\text{M}}$, respectively. The statistical evolutions of these deformation mechanisms are in detail discussed elsewhere as a function of microstructure and applied strain path [9]. Here, we focus on the nature of the damage incidents, and on the role of the local microstructure in the nucleation and growth of these cracking incidents.

5.2. Damage nucleation and growth

Examples of nucleation and evolution of different damage mechanisms are shown in Fig. 7a as a function of global strain. Associated local strains are also shown in red. It is observed here from these examples that all mechanisms may be activated at similar strain levels, but upon nucleation lead to different crack morphologies and final local strains. For example, the **F/F** damage mechanisms develop along grain boundaries to have higher aspect ratios and relatively lower associated strain compared to **M** or **M/F** damage mechanisms. These and other trends are quantitatively displayed for ferrite-dominated (**F** & **F/F**) and martensite-dominated (**M** & **M/F**) damage mechanisms in Fig. 7b: (i) The ferrite-dominated damage incidents nucleate at similar strain levels, but are fewer in quantity than martensite-dominated incidents. (ii) When nucleated at the same global strain, although ferrite-dominated damage incidents propagate faster, they cause relatively lower local strain at the onset

of failure compared to martensite-dominated incidents. This observation suggests a lower growth rate for ferrite-dominated damage incidents, which confirms the hypothesis put forward in [9] on the role of ferrite damage processes in ‘delocalizing’ the localized deformation through initiating a more dispersed strain hardening response. (iii) Damage incidents nucleated at higher global strain exhibit higher local strain at nucleation and lower local strain at onset of failure. This is more obvious in cases of **F** and **F/F** damage mechanisms (see the examples in Fig. 7a).

5.3. Damage nucleation mechanisms

Next, we examine each damage mechanism separately to reveal the dominating underlying factors that govern their nucleation. Fig. 8a and Fig. 8b–d show the critical strain, i.e., local equivalent strains at damage nucleation, for the bulk and interface-dominated damage mechanisms, respectively. Here the critical strain values represent the worst possible case, rather than the mean. As the critical strain also depends on the global strain, the following discussion, e.g. in each sub-figure of Fig. 8, is made among incidents with equal global strain at damage nucleation. In addition, incidents with similar neighboring (up to $\sim 4 \mu\text{m}$ distance) microstructure and strain fields are selected.

For bulk damage mechanisms, as would be expected, the lowest observed strain of **F** damage⁷ is much higher than that of **M** damage (Fig. 8a). In contrast to the difference between bulk damage mechanisms **F** and **M**, the difference between the critical strain of various interface-dominated damage mechanisms is smaller (e.g. compare Fig. 8b, Fig. 8c and Fig. 8d to each other). However, the critical strain trends presented in Fig. 8 separately for **F/F** (Fig. 8b), **M/F/M** (Fig. 8c) and $\text{M}^{\text{E}/\text{M}}$ (Fig. 8d) suggest that the interface-dominated damage processes are strongly governed by the local microstructure morphology and phase percolation. This further underlines the importance of the local microstructure dependence of the stress level [74] and stress state [83] at interfaces. These effects will be discussed in detail below.

⁷ It should be noted that only one ferrite bulk damage incident is detected. Cracking within the bulk of ferrite is extremely rare in DP steel, but we have confirmed with 3D characterization that there is no martensite or inclusion nearby this incident.

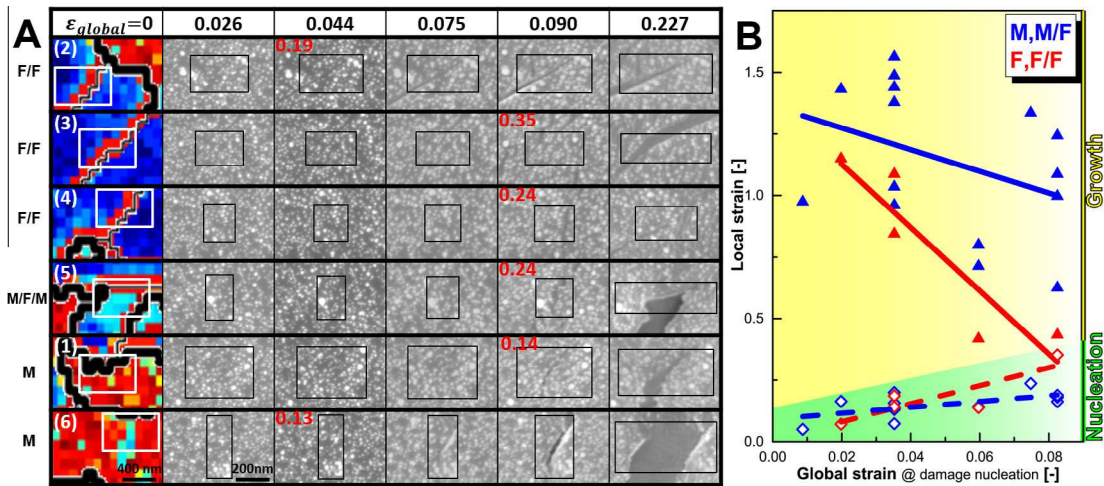


Fig. 7. Examples of damage mechanisms in DP steel and their local effects: (a): In-lens SE images of the nucleation and evolution of different damage mechanisms which are illustrated by corresponding boundary maps overlaid with the GND density (red number is the local strain at damage nucleation); (b): Local strain associated with martensite-dominated damage incidents (M, M/F; blue) and ferrite-dominated damage mechanisms (F, F/F; red), at damage nucleation (diamond markers) and at global failure (triangle markers) as a function of global strain. Dashed and full lines are drawn as guides to the eye to underline that although nucleation strains are similar, the final associated local strain with martensite-related damage incidents is higher. (For interpretation of the references to color in this figure legend, the reader is referred to the web version of this article.)

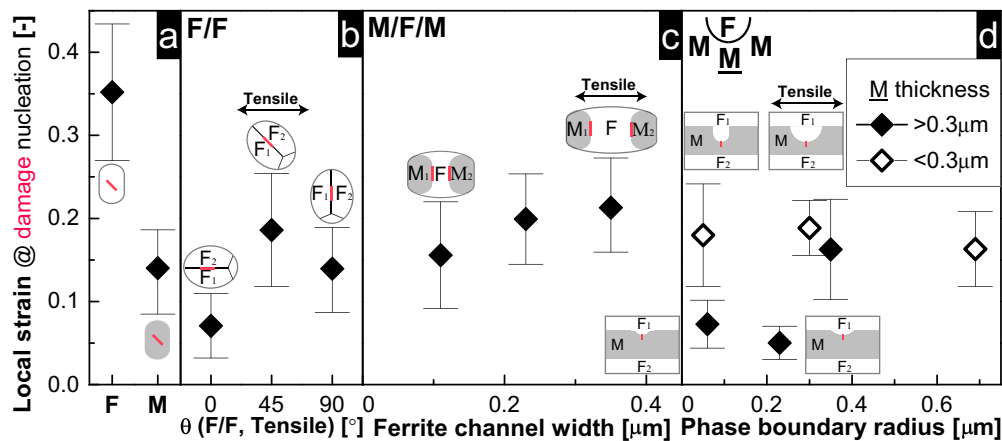


Fig. 8. Local strain at damage nucleation in DP steel of different damage mechanisms with respect to: (a) damage inside ferrite grains F or inside martensite islands M; (b) average angle θ between ferrite grain boundary segment and tensile direction ($\pm 5^\circ$) for ferrite grain boundary F/F damage; (c) ferrite channel width for martensite/ferrite phase boundary M/F damage; and (d) phase boundary radius at different bridging martensite M thickness for M/F damage. Corresponding microstructures are shown topologically.

5.3.1. Damage nucleation at ferrite/ferrite grain boundaries

Here we analyze the F/F damage mechanism. In Fig. 9, the evolution of local plastic strain and the GND density⁸ are given for an area cropped from the examined area shown in Fig. 5. The ferrite grain boundary in Fig. 9 with damage sites 1–4 is studied as an example. As observed in Fig. 7 (see 2, 3 and 4), the critical strain at damage nucleation at these sites varies, although they are located on the same ferrite grain boundary. This observation suggests a stress-controlled process, which is confirmed by consideration of the sequence of damage nucleation: Fig. 7a₂ shows that F/F damage incident 2, being closer to the F/M triple junction than e.g. incident 3, experiences higher strain hardening (indicated by the higher strain-induced GND density in Fig. 9c₃) and, hence, nucleates earlier.

⁸ In Fig. 9, the absolute value of deformation-induced GND density calculated from the plastic strain gradient is higher than the total GND density calculated from the orientation gradient. Compared to the full orientation tensor used for the total GND density calculation, due to the limitation of 2D strain measurement, 2 out of 5 independent components of strain tensor are missing when calculating the deformation induced GND, which explains this inconsistency.

In regions where the local stress is smaller, e.g. due to a smaller convex radius of the martensite at the M/F triple junction, the critical strain is observed to increase. An example of this is seen for the F/F damage incident 4 with a lower strain-induced GND density (Fig. 9c₃) and higher critical strain (Fig. 7a₄).

Another parameter investigated for the class of F/F damage incidents is the role of the grain boundary inclination (θ) with respect to the applied load [84,85]. Fig. 8b demonstrates that $\sim 45^\circ$ inclined F/F boundary segments experience higher critical strain than those less inclined. This is proposed to be due to two factors. First, the $\sim 45^\circ$ inclined segments have higher resolved-F/F-shear stress. Second, the resolved-F/F-shear stress gradient along the wavy segment is positively correlated to $|\cos(2\theta)|$, and thus it leads to a situation that $\sim 45^\circ$ inclined segments have lower stress gradients. These two facts lead to lower strain and strain gradient hardening, and in turn to a higher critical strain at the $\sim 45^\circ$ inclined segment. Thus, better overall ductility may be expected when increasing the ferrite grain boundary fraction inclined $\sim 45^\circ$ to the loading direction.

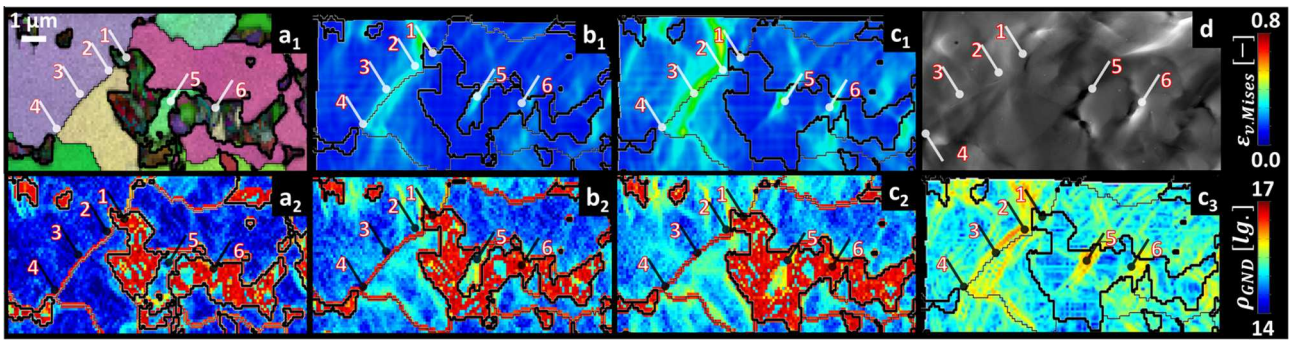


Fig. 9. Local strain and GND density evolution for the region (cropped from Fig. 5) of which the EBSD map is shown in (a₁) at (a) 0, (b) 0.04 and (c) 0.08, and (d) 0.23 global strain. The evolution of local strain is presented in (b,c₁), resulting damage incidents in (d), and the evolution of total GND density is shown in (a,b,c₂), corresponding deformation-induced part of (c₂) in (c₃).

5.3.2. Damage mechanisms at martensite/ferrite interfaces

Fig. 8c shows that as the ferrite channel width decreases, critical strain decreases. As the channel width increases, the strain gradient, including the inherited transformation misfit strain gradient [15], and in turn the total GND density decreases. This will lead to an increased critical strain. These topological observations, underline limitations in ductility for DP steels with decreased martensite dispersion for a given martensite volume fraction.

Fig. 8d reveals the effect of the martensite notch characteristics: both bridging martensite thickness and notch radius affect the critical strain required for damage. When the bridging martensite is thicker than 0.3 μm , the critical strain decreases as the M/F interface notch radius decreases, due to an increased stress intensity factor. However, this rule does not hold for the thinner bridging martensite, where the notch effect is weakened by the strong multilayer effect which enhances the bridging martensite ductility through the overlaid ferrite at such positions [83]. Thus, increasing the concave radius or reducing the thickness of the dispersed martensite will enhance the damage resistance of the M/F boundary regions.

6. Summary and conclusions

We presented a novel approach that enables joint high-resolution mapping of deformation-induced evolution of microstructures and microstrains with the aim to better understand the microstructure dependence of damage initiation in dual phase steels. The approach relies on (1) scanning electron microscopy based imaging techniques, namely, electron backscatter diffraction, electron channeling contrast imaging, etc., to map the microstructure evolution such as changes in phase morphologies, defect densities, crystallographic orientation, and the nucleation of damage incidents, and on (2) nanoparticle-based microscopic-digital image correlation technique to map microstrain evolution. The novelty of the approach lies in the concurrent possibility of *selective (microstructure-independent) pattern imaging* and *selective (pattern-independent) microstructure imaging* conditions achieved by careful optimization of scanning electron microscopy imaging conditions. These conditions enable high-resolution mapping of both fields, revealing the topological, microstructural and thus micromechanical conditions for damage nucleation.

Application of this methodology to the case of ferrite/martensite dual-phase steel reveals the value of such high resolution, high-stability $\mu\text{-DIC}$ approaches since the strain is observed to be severely localized even within ferritic grains. It also underlines the strength of direct coupling micromechanical mapping to the actual underlying microstructure evolution, since such coupled

approaches are crucial in identifying the true nature of deformation and damage mechanisms in such multi-phase microstructures. The case study presented here revealed that damage nucleation in dual-phase steel is in most cases not strain controlled, and that it is most strongly dependent on the local martensite morphology and percolation. In this regard, four specific microstructure design guidelines are proposed to produce damage-resistant dual phase steels, which are based on optimizing (i) ferrite grain boundary inclination relative to the loading direction; (ii) martensite distribution; (iii) bridging martensite radius and (iv) bridging martensite thickness.

Acknowledgments

The authors would like to thank Monika Nellesen and Michael Adamek for their support with the experiments. The financial support by the European Union via the ERC advanced grant “SmartMet”, and from the International Max Planck Research School for Surface and Interface Engineering in Advanced Materials (IMPRS-SurMat) is also gratefully acknowledged.

Appendix A. Optimization of particle type, distribution and imaging

The μE & μS mapping methodology requires three conditions: Criterion A necessitates the use of particles that are well-below the micrometer scale in size, and those which can also be well-dispersed on the sample surface, to achieve high spatial strain resolution; Criterion B necessitates limiting the microstructure manipulation, and the microstructure imaging influence of the pattern, to achieve selective microstructure imaging; and Criterion C necessitates optimized SEM imaging conditions for low-interaction volume imaging with minimized edge and charging effects, to achieve selective pattern imaging.

To fulfill conditions A and B, nano-sized, chemically-inert particles are to be determined and then dispersed on the specimen surface at room temperature as a single layer. Ceramic nanoparticles are in general suitable for this purpose due to their low effective atomic number, that provide weak elastic scattering of high energy electrons, i.e., low BSE yield. Among possible options, SiO_2 is chosen here due to a number of advantages: These are good adherence; higher transparency to the electron-beam with respect to crystalline noble metal nanoparticles due to the amorphous structure; better low-kV imaging with respect to noble metal due to much lower upper neutrality energy; and broad availability. In this study, colloidal silica (Microdiamant GmbH, Germany) with a size of $34 \text{ nm} \pm 29 \text{ nm}$ is employed.

Table A1Detailed procedure for dispersing the SiO₂ nanoparticles on the sample surface.

Step	Goal
1 The sample surface is metallographically prepared to colloidal silica (OPS) final finish.	A deformation-free surface finish is achieved.
2 On a clean polishing cloth plate 10–20 drops of OPS are placed along the diameters	SiO ₂ particles are evenly distributed in the cloth.
3 Sample is pressed with 1–2 MPa pressure on the cloth, and rotated at 2 RPS for 1 s.	SiO ₂ particles are transferred to the sample surface.
4 With water flushing and 100 RPS plate speed, the sample is rotated on the cloth with 1–2 MPa pressure at 2 RPS for 3 s.	A SiO ₂ monolayer is formed and larger SiO ₂ particles are removed from the surface.
5 Sample surface is rinsed with ethanol, and dried by an air fan.	Floating particles are removed.

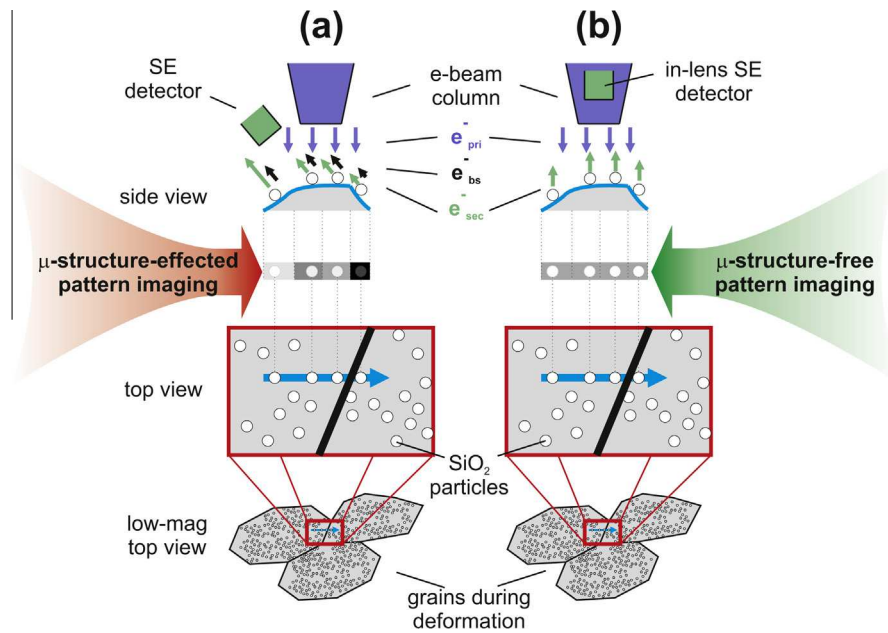


Fig. A1. Schematic representation of the microstructure-independent pattern imaging methodology in (b), with respect to conventional SE detector imaging in (a). Upon the use of an in-lens SE detector setup with minimized interaction volume conditions topographic information from microstructure (arising due to pile-up at a grain boundary) is avoided, and the selective pattern imaging can be accomplished. Note that in (b) backscattered electrons are created, however, these are filtered out (as explained in the text) and do not contribute to the final image.

A challenge in employing SiO₂ nanoparticles lies in the difficulty to achieve good dispersion on the polished specimen surface without the formation of larger agglomerates. In fact, in preliminary tests this could not be achieved by several existing coating methods, such as spin coating, spray coating, drop casting and dip coating. Thus a novel room temperature drop casting method is developed, that ensures optimal dispersion of the nanoparticles as a single layer. The individual steps of this protocol are summarized in Table A1. This procedure has the additional advantage that the mean particle size is reduced by the preferential removal of the larger SiO₂ particles.

To fulfill condition C, i.e. microstructure-independent pattern imaging, SEM beam and detector parameters need to be optimized to minimize (a) the topological contrast arising from slip steps, grain rotations, damage etc. and (b) the interaction volume to the size of nanoparticles. The followed strategy is schematically shown in Fig. A1, and described in detail in next.

In order to minimize the former, topological contrast, the depth-of-field is increased by using a smaller objective aperture (30 μm). Removal of topological effects arising from surface tilt with respect to detector position, which is the other major factor creating the topological contrast, is more challenging. The working distance can be increased for this purpose, however, this would reduce resolution and therefore is kept in this work instead at

6 mm. Here we propose an alternative strategy that simultaneously reduces the electron beam interaction volume and the angle between SE detector and the axis of electron column, two factors that both reduce topographic contrast arising from surface tilt: Instead of a SE detector, an in-lens SE detector is used. The typically used combined SE signal is actually formed by the individual SE1, SE2 and SE3 signals. Compared to the conventional SE detector which mainly detects higher energy SE2, the in-lens SE detector mostly detects the low energy SE1 due to trajectory filtering and the subsequent ExB filtering [86,87]. Since the SE1 signal provides the highest spatial resolution and lowest penetration depth, and the in-lens SE detector is fully-aligned with the axis of the electron column, surface tilt induced topological contrast can be significantly reduced. The effect is schematically shown in Fig. A1.

To minimize the interaction volume, apart from the contribution from the use of the in-lens SE detector explained above, the acceleration voltage and beam current can be lowered. However, lowering acceleration voltage also decreases spatial resolution and increases charging-induced particle shape distortion. Thus, in the ideal case the acceleration voltage should be limited around the upper neutrality voltage. We realize these conditions by decreasing the aperture size from 120 μm to 30 μm, the acceleration voltage from 15 kV to 1.5 kV and switching off the high beam current mode.

References

- [1] M. Calcagnotto, Y. Adachi, D. Ponge, D. Raabe, *Acta Mater.* 59 (2011) 658.
- [2] K. Davut, S. Zaeferrer, *Steel Res. Int.* 83 (2012) 584.
- [3] I. Gutierrez-Urrutia, D. Raabe, *Scr Mater.* 68 (2013) 343.
- [4] D. Raabe, D. Ponge, O. Dmitrieva, B. Sander, *Adv. Eng. Mater.* 11 (2009) 547.
- [5] D. Banerjee, J.C. Williams, *Acta Mater.* 61 (2013) 844.
- [6] H. Gao, K. Ikeda, T. Morikawa, K. Higashida, H. Nakashima, *Mater. Trans.* 54 (2013) 632.
- [7] G. Avramovic-Cingara, Y. Ososkov, M.K. Jain, D.S. Wilkinson, *Mater. Sci. Eng. A* 516 (2009) 7.
- [8] K.S. Choi, W.N. Liu, X. Sun, M.A. Khaleel, *Metall. Mater. Trans. A* 40 (2009) 796.
- [9] J.P.M. Hoefnagels, C.C. Tasan, F.J. Peters, F. Maresca, V.G. Kouznetsova, *J. Mater. Sci.* Accepted for publication.
- [10] J. Kang, Y. Ososkov, J.D. Embury, D.S. Wilkinson, *Scr. Mater.* 56 (2007) 999.
- [11] E. Maire, O. Bouaziz, M. Di Michiel, C. Verdu, *Acta Mater.* 56 (2008) 4954.
- [12] X. Sun, K.S. Choi, A. Soulam, W.N. Liu, M.A. Khaleel, *Mater. Sci. Eng. A* 526 (2009) 140.
- [13] X. Sun, K.S. Choi, W.N. Liu, M.A. Khaleel, *Int. J. Plast.* 25 (2009) 1888.
- [14] C.C. Tasan, M. Diehl, D. Yan, C. Zambaldi, P. Shanthraj, F. Roters, D. Raabe, *Acta Mater.* 81 (2014) 386.
- [15] M. Calcagnotto, D. Ponge, E. Demir, D. Raabe, *Mater. Sci. Eng. A* 527 (2010) 2738.
- [16] I. Gutierrez-Urrutia, D. Raabe, *Scr. Mater.* 66 (2012) 343.
- [17] S. Zaeferrer, N.-N. Elhami, *Acta Mater.* 75 (2014) 20.
- [18] B. Pauwels, X. Liu, A. Sasov, X-Ray Nanotomography in a SEM, in: S.R. Stock (Ed.), *Proc SPIE*, vol. 7804, 2010.
- [19] C.C. Tasan, J.P.M. Hoefnagels, M.G.D. Geers, *Scr. Mater.* 62 (2010) 835.
- [20] P. Villechaise, J. Mendez, P. Violan, *Mater. Sci. Eng. A* 141 (1991) L9.
- [21] G.S. Tzeng, H.J. Chen, Y.Y. Wang, C.C. Wan, *Surf. Coat. Technol.* 89 (1997) 108.
- [22] W. Guo, E. Jägle, J. Yao, V. Maier, S. Korte-Kerzel, J.M. Schneider, D. Raabe, *Acta Mater.* 80 (2014) 94.
- [23] B.-C. Ng, B. Simkin, M.A. Crimp, Examination of Dislocation Structures Near Crack TIP Region of B2 NiAl Alloys, in: *Symp. Z – High-Temp. Ordered Intermet. Alloys VII*, vol. 460, 1996.
- [24] E. Plancher, C.C. Tasan, S. Sandloebes, D. Raabe, *Scr. Mater.* 68 (2013) 805.
- [25] I. Gutierrez-Urrutia, S. Zaeferrer, D. Raabe, *JOM* 65 (2013) 1229.
- [26] I. Gutierrez-Urrutia, D. Raabe, *Scr. Mater.* 69 (2013) 53.
- [27] I. Gutierrez-Urrutia, S. Zaeferrer, D. Raabe, *Mater. Sci. Eng. A* 527 (2010) 3552.
- [28] E.E. Patterson, D.P. Field, Y. Zhang, *Mater. Charact.* 85 (2013) 100.
- [29] R. Guo, T. Hang, D. Mao, M. Li, K. Qian, Z. Lv, H. Chiu, *J. Alloys Compd.* 588 (2014) 622.
- [30] Y. Chen, J. Hjelen, H.J. Roven, *Trans. Nonferrous Met. Soc. China* 22 (2012) 1801.
- [31] P. Yang, *J. Chin. Electron. Microsc. Soc.* 27 (2008) 425.
- [32] T. Fukino, S. Tsunekawa, *Mater. Trans.* 49 (2008) 2770.
- [33] L. Ryde, J. Hagström, W.B. Hutchinson, *Mater. Sci. Forum* 550 (2007) 321.
- [34] G.K. Tirumalasetty, M.A. van Huis, C. Kwakernaak, J. Sietsma, W.G. Sloof, H.W. Zandbergen, *Acta Mater.* 60 (2012) 1311.
- [35] J. Jiang, T.B. Britton, A.J. Wilkinson, *Acta Mater.* 61 (2013) 7227.
- [36] A.-L. Helbert, W. Wang, F. Brisset, T. Baudin, R. Penelle, *Adv. Eng. Mater.* 14 (2012) 39.
- [37] P.A. Lynch, D. Tomus, C.J. Bettles, M.A. Gibson, A.W. Stevenson, *Nucl. Instrum. Methods Phys. Res. Sect. Accel. Spectrometers Detect. Assoc. Equip.* 619 (2010) 298.
- [38] H. Li, C.J. Boehlert, T.R. Bieler, M.A. Crimp, *Philos. Mag.* 92 (2012) 2923.
- [39] L. Allais, M. Bornert, T. Bretheau, D. Caldemaison, *Acta Metall. Mater.* 42 (1994) 3865.
- [40] M. Sutton, W. Wolters, W. Peters, W. Ranson, S. McNeill, *Image Vis Comput.* 1 (1983) 133.
- [41] M.A. Sutton, F. Hild, H. Jin, X. Li, M.M. Grédiac, *Exp. Mech.* 51 (2011) 401.
- [42] D. Raabe, M. Sachtleber, Z. Zhao, F. Roters, S. Zaeferrer, *Acta Mater.* 49 (2001) 3433.
- [43] D. Raabe, M. Sachtleber, H. Weiland, G. Scheele, Z. Zhao, *Acta Mater.* 51 (2003) 1539.
- [44] Z. Zhao, M. Ramesh, D. Raabe, A.M. Cuitiño, R. Radovitzky, *Int. J. Plast.* 24 (2008) 2278.
- [45] J. Kang, M. Jain, D.S. Wilkinson, J.D. Embury, *J. Strain Anal. Eng. Des.* 40 (2005) 559.
- [46] K.N. Jonnalagadda, I. Chasiotis, S. Yagnamurthy, J. Lambros, J. Pulskamp, R. Polcawich, M. Dubey, *Exp. Mech.* 50 (2010) 25.
- [47] S. Cho, J.F. Cárdenas-García, I. Chasiotis, *Sens. Actuators Phys.* 120 (2005) 163.
- [48] A. Weidner, A. Yanina, S. Guk, R. Kawalla, H. Biermann, *Steel Res. Int.* 82 (2011) 990.
- [49] H. Ghadbeigi, C. Pinna, S. Celotto, J.R. Yates, *Mater. Sci. Eng. A* 527 (2010) 5026.
- [50] M. Kapp, T. Hebesberger, O. Kolednik, *Int. J. Mater. Res. Former Z. Fuer. Met.* 102 (2011) 687.
- [51] R. Mishra, R. Kubic, *Microsc. Microanal.* 14 (2008) 552.
- [52] Q. Han, Y. Kang, P.D. Hodgson, N. Stanford, *Scr. Mater.* 69 (2013) 13.
- [53] P. Shade, M. Groeber, M. Uchic, R. Wheeler, *Microsc. Microanal.* 18 (2012) 720.
- [54] M. Sebastiani, C. Eberl, E. Bemporad, G.M. Pharr, *Mater. Sci. Eng. A* 528 (2011) 7901.
- [55] J. Marteau, H. Haddadi, S. Bouvier, *Exp. Mech.* 53 (2013) 427.
- [56] G. Martin, C.W. Sinclair, J.-H. Schmitt, *Scr. Mater.* 68 (2013) 695.
- [57] T. Morikawa, Y. Mitani, K. Higashida, *Mater. Sci. Forum* 638–642 (2010) 1574.
- [58] Y. Tanaka, K. Naito, S. Kishimoto, Y. Kagawa, *Nanotechnology* 22 (2011) 115704.
- [59] W.A. Scrivens, Y. Luo, M.A. Sutton, S.A. Collette, M.L. Myrick, P. Miney, P.E. Colavita, A.P. Reynolds, X. Li, *Exp. Mech.* 47 (2007) 63.
- [60] F.D. Gioacchino, J.Q. da Fonseca, *Exp. Mech.* 53 (2012) 743.
- [61] S.-H. Joo, J.K. Lee, J.-M. Koo, S. Lee, D.-W. Suh, H.S. Kim, *Scr. Mater.* 68 (2013) 245.
- [62] H. Jin, W.-Y. Lu, J. Korellis, *J. Strain Anal. Eng. Des.* 43 (2008) 719.
- [63] F. Di Gioacchino, W.J. Clegg, *Acta Mater.* 78 (2014) 103.
- [64] A.D. Kammers, S. Daly, *Meas. Sci. Technol.* 22 (2011) 125501.
- [65] M.D. McMurtrey, G.S. Was, B. Cui, I. Robertson, L. Smith, D. Farkas, *Int. J. Plast.* 56 (2014) 219.
- [66] M. Krottenthaler, C. Schmid, J. Schaufler, K. Durst, M. Göken, *Surf. Coat Technol.* 215 (2013) 247.
- [67] Y. Huh, K.J. Hong, K.S. Shin, *Microsc. Microanal.* 19 (2013) 33.
- [68] Š. Mikmeková, K. Matsuda, K. Watanabe, S. Ikeno, I. Müllerová, L. Frank, *Mater. Trans.* 52 (2011) 292.
- [69] Z. Sun, J.S. Lyons, S.R. McNeill, *Opt. Lasers Eng.* 27 (1997) 409.
- [70] J. Lackmann, T. Niendorf, M. Maxisch, G. Grundmeier, H.J. Maier, *Mater. Charact.* 62 (2011) 298.
- [71] T. Niendorf, J. Lackmann, B. Gorny, H.J. Maier, *Scr. Mater.* 65 (2011) 915.
- [72] C.J. Ruesing, T. Niendorf, J. Lackmann, A. Frehn, H.J. Maier, *Int. J. Mater. Res.* 103 (2012) 12.
- [73] T.A. Berfield, J.K. Patel, R.G. Shimmin, P.V. Braun, J. Lambros, N.R. Sottos, *Exp. Mech.* 47 (2007) 51.
- [74] N.A. Fleck, G.M. Müller, M.F. Ashby, J.W. Hutchinson, *Acta Metall. Mater.* 42 (1994) 475.
- [75] E. Demir, D. Raabe, N. Zaafarani, S. Zaeferrer, *Acta Mater.* 57 (2009) 559.
- [76] C.C. Tasan, J.P.M. Hoefnagels, M. Diehl, D. Yan, F. Roters, D. Raabe, *Int. J. Plast.* 63 (2014) 198.
- [77] S. Choi, S.P. Shah, *Exp. Mech.* 37 (1997) 307.
- [78] L. Larsson, M. Sjö Dahl, F. Thuvander, *Opt. Lasers Eng.* 41 (2004) 767.
- [79] D. Lei, F. Hou, X. Gong, *Exp. Tech.* 36 (2012) 24.
- [80] G. Zhang, D. Liang, J.-M. Zhang, *Comput. Geotech.* 33 (2006) 248.
- [81] F. Lagattu, F. Bridier, P. Villechaise, J. Brillaud, *Mater. Charact.* 56 (2006) 10.
- [82] C. Rehr, S. Kleber, T. Antretter, R. Pippan, *Mater. Charact.* 62 (2011) 793.
- [83] D. Yan, C.C. Tasan, D. Raabe, *Acta Mater.* Submitted for publication.
- [84] T.R. Bieler, P. Eisenlohr, F. Roters, D. Kumar, D.E. Mason, M.A. Crimp, D. Raabe, *Int. J. Plast.* 25 (2009) 1655.
- [85] F. Roters, P. Eisenlohr, L. Hantcherli, D.D. Tjahjanto, T.R. Bieler, D. Raabe, *Acta Mater.* 58 (2010) 1152.
- [86] B. Griffin, D. Joy, J. Michael, *Microsc. Microanal.* 15 (2009) 46.
- [87] K. Kumagai, T. Sekiguchi, *Ultramicroscopy* 109 (2009) 368.